OCTRA as Ultrasonically Absorptive Thermal Protection Material for Hypersonic Transition Suppression

V. Wartemann[1], A. Wagner[2], D. Surujhlal[3], C. Dittert[4]

Abstract

Previous investigations in the High Enthalpy Shock Tunnel Göttingen (HEG) of the German Aerospace Center (DLR) show that carbon fiber reinforced carbon ceramic (C/C) surfaces can be utilized to damp hypersonic boundary layer instabilities resulting in a delay of boundary layer transition onset. Numerical stability analyses confirmed these experimental results. However, C/C has some disadvantages, especially the limited oxidation resistance and its low mechanical strength, which could be critical during hypersonic flights. Thus, an ultrasonically absorptive fiber reinforced ceramic material based on a silicon carbide (C/C-SiC) was developed in the past years to fulfill this need. The present paper addresses the numerical rebuild of the C/C-SiC absorber properties using impedance boundary conditions together with linear stability analysis. The focus of this paper is on the numerical comparison of the original C/C material and the improved C/C-SiC material, referred to as OCTRA in the literature. The influence on the second modes and the transition itself is investigated. The numerical results are compared with HEG wind tunnel tests. The wind tunnel model tested in HEG is a 7° half-angle blunted cone with an overall model length of about 1.1 m and a nose tip radius of 2.5 mm. These experiments were performed at Mach 7.5 and at different freestream unit Reynolds numbers.

Keywords: *Ultrasonically Absorptive Thermal Protection Material, Hypersonic Transition Suppression, Stability Analyses, Second Mode Instability, High Enthalpy Shock Tunnel Göttingen (HEG)*

1. Introduction

The increase of the laminar portion of a boundary layer is of critical importance to the design and optimization of future hypersonic transport vehicles. This motivates the development of concepts to control hypersonic boundary layer transition. In the present paper an ultrasonically absorptive porous coating with random microstructure is used to passively control boundary layer transition.

The second mode instability, commonly referred to as Mack mode [1], is the dominant mode for essentially 2D boundary layers at high local Mach number ($Ma_e > 4$) and/or cold walls. A strong stabilization effect of the second mode instability above porous surface models with regular, cylindrical pores was shown theoretically and experimentally by Fedorov et al. [2] and Rasheed et al. [3]. Analogous results were presented by Fedorov et al. [4], Maslov et al. [5, 6] and Lukashevich et al. [7] who investigated randomly structured felt metal. First studies with randomly structured carbon-carbon ceramic (C/C) were conducted by Wagner et al. [8] in the HEG and were compared with numerical LST predictions by Wartemann et al. [9]. In all cases a stabilization effect on the second mode instability was observed, resulting in a significant delay of transition onset. The starting material C/C (Wagner et al. [8]) has two main disadvantages: its limited oxidation resistance and the low mechanical strength, which could

---

[1] *German Aerospace Center (DLR), Spacecraft Department, Institute of Aerodynamics and Flow Technology, Braunschweig, Germany, Viola.Wartemann@dlr.de*

[2] *German Aerospace Center (DLR), Spacecraft Department, Institute of Aerodynamics and Flow Technology, Göttingen, Germany, Alexander.Wagner@dlr.de*

[3] *German Aerospace Center (DLR), Spacecraft Department, Institute of Aerodynamics and Flow Technology, Göttingen, Germany, Divek.Surujhlal@dlr.de*

[4] *German Aerospace Center (DLR), Space System Integration Department, Institute of Structures and Design, Stuttgart, Germany, Hendrik.Weihs@dlr.de*

be critical for real hypersonic flight applications. Carbon fiber reinforced silicon carbide (C/C-SiC) is highly suitable as thermal protection material (TPS) and was successfully tested as TPS during multiple flight test programs [10–12]. This dense C/C-SiC TPS material was not developed for the application as an acoustic absorber. To close the gap between the porous C/C and the dense C/C-SiC, a new material based on C/C-SiC was developed [13], [14]. Contrary to the dense C/C-SiC materials, the new C/C-SiC material, also known as OCTRA (Optimized Ceramic for Hypersonic Applications), has a porosity and permeability like C/C. The present paper addresses the numerical rebuild of the OCTRA absorber behaviour using an impedance boundary conditions together with linear stability analysis. The numerical results are compared with wind tunnel tests, which were performed in the HEG at Mach 7.5 and different unit Reynolds numbers. A 7° half-angle cone model with a nose radius of 2.5 mm and a total length of about 1.1 m was used. The measurements are compared with the numerical calculations of the original C/C material and the improved OCTRA material. The influence on the second modes and the transition itself are investigated.

2. Numerical methods

In the first subsection 2.1 a brief description of base flow calculations is given. The second subsections 2.2 summarizes the stability code itself, including the implemented boundary conditions for the porous material.

2.1. Mean flow solver

For the base flows $\bar{q}$ calculations the DLR TAU code is used. The code is a three-dimensional parallel hybrid multi-grid code and has been validated for hypersonic flows (see e.g. Mack et al. [15], Schwamborn et al. [16] or Reimann et al. [17]). The grids are axisymmetric. Previous analyses [18] have shown, that the base flow simulations should include the nozzle, test chamber and cone model, which is consequently applied. For all grids, grid clustering towards the walls as well as around the shock is applied. For the near-field cone a structured grid is used, with 654 grid points in streamwise direction and 350 grid points in wall normal direction. A grid study can be found for example in Wartemann et al. [18]. Based on the nozzle calibration of Wagner [19], the nozzle boundary layer is set turbulent, which is modelled with the Spalart-Allmaras turbulence model. The model wall temperature for all tests is assumed to be isothermal at 293 K, which is appropriate for the HEG test times.

2.2. Stability code

The stability analysis is performed with the stability code NOLOT (NOnLocal Transition analysis, Hein [20]), which was developed in cooperation between the DLR and the Swedish Defence Research Agency. The equations are derived from the conservation equations of mass, momentum and energy, which govern the flow of a viscous, compressible, ideal gas. All flow and material quantities are decomposed into a steady laminar base flow $\bar{q}$ and an unsteady disturbance flow $\tilde{q}$

$$q(x_c, y_c, z_c, t) = \bar{q}(x_c, y_c) + \tilde{q}(x_c, y_c, z_c, t). \tag{1}$$

As mentioned above, the laminar base-flow $\bar{q}$ is calculated by the DLR TAU code. The disturbance $\tilde{q}$ of equation 1 is represented as a harmonic wave

$$\tilde{q}(x_c, y_c, z_c, t) = \hat{q}(x_c, y_c, z_c) \exp[i(\alpha x_c + \beta z_c - \omega t)] \tag{2}$$

with the complex-valued amplitude function $\hat{q}$. The three coordinate directions of the equations 1 and 2 are denoted as x_c, y_c and z_c and describe a curvilinear surface-oriented orthogonal coordinate system. The NOLOT code can be used for local as well as non-local analyses. In the range of this paper the local linear spatial approach is used, which is a subset of the non-local stability equations. Previous investigations of the same geometry with a similar free stream condition, based on a comparison of the experimental / calculated growth rate of the second modes, shows that it is possible to apply LST (linear stability theory) instead of PSE (Parabolized Stability Equations), see e.g. Wartemann [21].

The boundary conditions in NOLOT for a smooth wall (at $y = 0$) are:

$$\hat{u}_w, \ \hat{v}_w, \ \hat{w}_w, \ \hat{T}_w = 0. \tag{3}$$

For the numerical rebuild of the experiments the stability code NOLOT is equipped with different impedance boundary conditions (see e.g. Wartemann et al. [9]). The general approach for all implemented conditions are, Maslov et al. [22]:

$$\hat{u}_w, \; \hat{w}_w, \; \hat{T}_w = 0, \quad \hat{v}_w = A\hat{p}_w, \tag{4}$$

where the subscript w denotes a value at the wall. The admittance A is calculated by

$$A = -\frac{n}{Z_0}\tanh(mh), \tag{5}$$

where n is the porosity and d the pore depth. The characteristic impedance Z_0 and the propagation constant m depends on the chosen approach. In NOLOT different approaches are implemented, see e.g. Wartemann et al. [23]. The applied boundary condition here is dependent on the material and acoustic properties: the porosity, thickness, length specific flow resistivity and structure factor (see for example Möser [24]). The original boundary condition is implemented with constant acoustic properties (see Wartemann et al. [23]). In this paper the acoustic properties are implemented as a function of the of disturbance wave frequency, which is described in the following section 3.1.

3. Experimental approach
The present section describes the material and acoustic properties of C/C as well as OCTRA material, the wind tunnel model, including parts of the layout, and the wind tunnel setup.

3.1. Material and acoustic properties
The main properties, which are necessary for the numerical analysis, are summarized in table 1.

**Table 1.** Applied material and acoustic properties for the numerical study.

material	porosity	structure factor	flow resistivity $[MPa \cdot s/m^2]$
C/C	14.9%	8	13.3
OCTRA	15.8%	$4.8E^{-12} \cdot f^2 - 5.3E^{-06} \cdot f + 2.3$	$1.6E^{-11} \cdot f^3 - 7.0E^{-06} \cdot f^2 + 0.9 \cdot f + 0.3E^6$

A detailed description of the C/C material properties can be found for example in Wartemann et al. [23]. Intermediate results of the optimized OCTRA can be found in Dittert et al. [13] and [14]. The structure factor as well as the specific flow resistivity are expressed as functions of disturbance wave frequency to adapt the homogenous absorber theory in the best way possible to the experimentally obtained reflection coefficients. Figure 1 provides the absorption coefficient distribution as a function of frequency and ambient pressure (or equivalent static/surface pressure in flight). The properties are based on the experimentally obtained absorption coefficients between 125 kHz and 490 kHz at static pressures of up to 15000 Pa. The provided distribution in figure 1 corresponds to the material properties expressed in table 1.

3.2. Wind tunnel and wind tunnel model
All tests were conducted in the High Enthalpy Shock Tunnel Göttingen (HEG). Originally, the facility was designed for the investigation of the influence of high temperature effects such as chemical and thermal relaxation on the aerothermodynamics of entry or re-entry space vehicles. In this operating range, total specific enthalpies of up to 23 MJ/kg and nozzle stagnation pressures of up to 150 MPa can be reached. In recent years its range of operating conditions has been subsequently extended allowing to study hypersonic boundary layer transition corresponding to hypersonic flight configurations ranging from low altitude Mach 6 up to Mach 10 at approximately 33 km altitude (see e.g. Hannemann et al. [25]).

In the scope of the present study HEG was operated using the conditions listed in table 2, i.e. in a free stream unit Reynolds number range from $Re_m = 1.4 \times 10^6$/m to $Re_m = 6.4 \times 10^6$/m and total enthalpies around 3 MJ/kg. Typical test times for these conditions range from 2.5 to 4 ms. The wind tunnel model tested in HEG is a 7° half-angle blunted cone with an overall sharp model length of 1100 mm and a nose
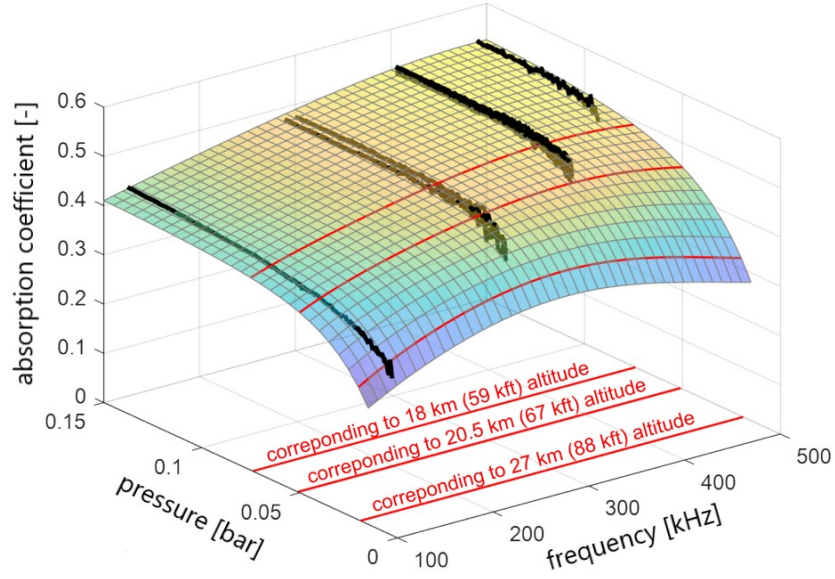
**Fig 1.** Absorption coefficient distribution of OCTRA.

Table 2. Mean HEG test conditions at Mach 7.5 of the presented study.

Re_m $[m^{-1}]$	1.4×10^6	4.0×10^6	6.4×10^6
p_0 $[MPa]$	6.7	19	28
T_0 $[K]$	2690	2720	2550
h_0 $[MJ/kg]$	3.2	3.2	3.0
T_∞ $[K]$	260	270	245
ρ_∞ $[g/m^3]$	10	28	42
u_∞ $[m/s]$	2400	2410	2340

tip radius of 2.5 mm. One third of the cone is equipped with an exchangeable insert which covers 122° of the model surface in the circumferential direction. The prior C/C insert starts at 182 mm from the model tip with a total length of 800 mm (see figure 2).
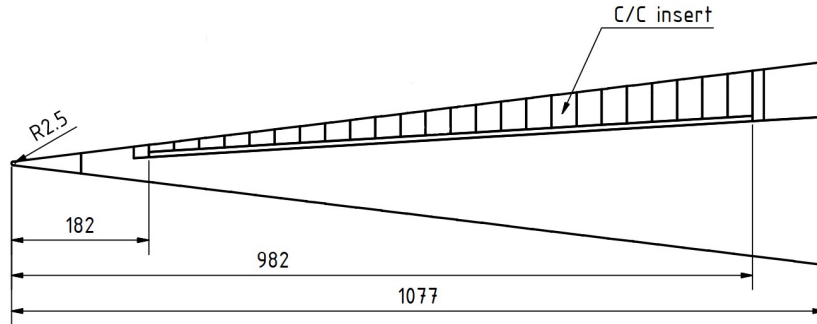
Fig 2. HEG wind tunnel model with exemplary C/C insert. All dimensions are provided in millimeter.

Additional a second insert was equipped with the improved OCTRA material. The length optimization of this resent insert is investigated in the next subsection 3.3.

For all numerical calculations, a porous layer thickness of 5 mm is used, which is (for the present test conditions) above the deep pore limit beyond which an additional absorber thickness does not further increase its effectiveness.

Further, the model was equipped with thermocouples for the detection of the transition location on the cone by evaluating the surface heatflux distribution. Additionally, PCB sensors and fast-response pressure transducers are grouped in pairs and flush mounted along the model. These pressure transducers are used to measure pressure fluctuations in the boundary layer occurring above the cone surface.

3.3. Length optimization for the OCTRA insert

This subsection addresses a possible reduction of the insert length for the recent OCTRA insert. The pre-analysis is based on an experiment with a similar cone geometry, which has the same dimensions as in the present project: a 7° half-angle blunted cone with a nose radius of 2.5 mm and a total length of about 1 m. An experimental test case with an unit Reynolds number of $Re_m = 6.4 \times 10^6$/m and a Mach number of 7.5 is chosen. For the LST transition prediction the semi-empirical approach of the e^N-method is applied. In figure 3 the results of the smooth surface side, marked by black lines, are visible: The measured transition x-coordinate are from a previous wind tunnel test campaign of the HEG (see Wagner [19] or Wartemann et al. [23]). The measured $x_{\text{trans,smooth}}$ results in a $N_{\text{trans,smooth}}$ of about 8.5 (see fig. 3). This N-factor is used for the following analysis.

Figure 4 shows the investigations for the reduction of the insert length: red lines are standing for a cone with porous material from 182 mm up to 1000 mm, which is the maximal possible insert length. Additionally, the N-factor distributions for an insert length of 400 mm up to 1000 mm is visible in fig. 4.a (blue lines) and ranging from 500 mm up to 1000 mm in fig. 4.b (orange lines). Only at the beginning of the cone are differences visible due to the variation of the insert beginning. In the rear of the cone, the distributions merge. This results in the same predicted transition start of about 0.82 m. The reason for this behavior is illustrated in figure 5.a, which shows the results of an insert ranging from 600 mm up to 1000 mm (green lines). Applying a boundary condition for the porous material, the chosen LST approach results in an abrupt change of the growth rates at the beginning of the insert (figure 5.a). Thus calculations based on PSE would be preferable. Nevertheless, the LST analysis can be used for its trend. The shorter selected insert length of fig. 5.b (green lines) results in a different predicted transition beginning, compared with a porous insert over almost the whole cone (red lines). To be on the safe side, the
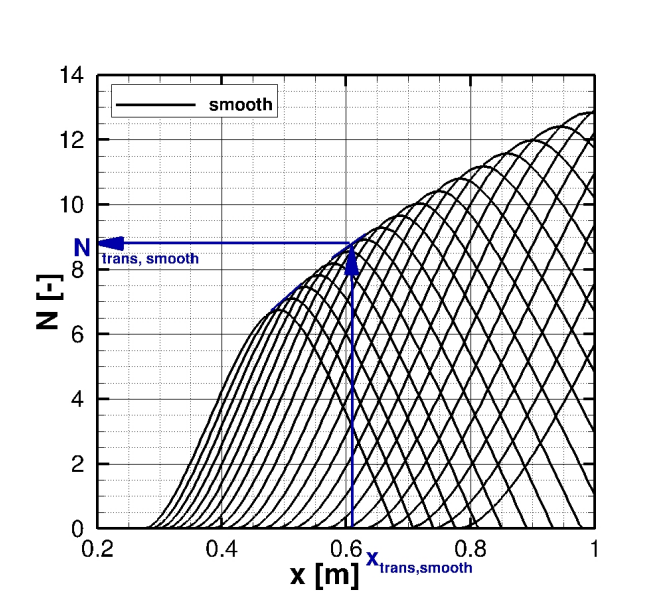
Fig 3. Semi-empirical approach of the e^N-method, $Re_m = 6.4 \times 10^6$/m.
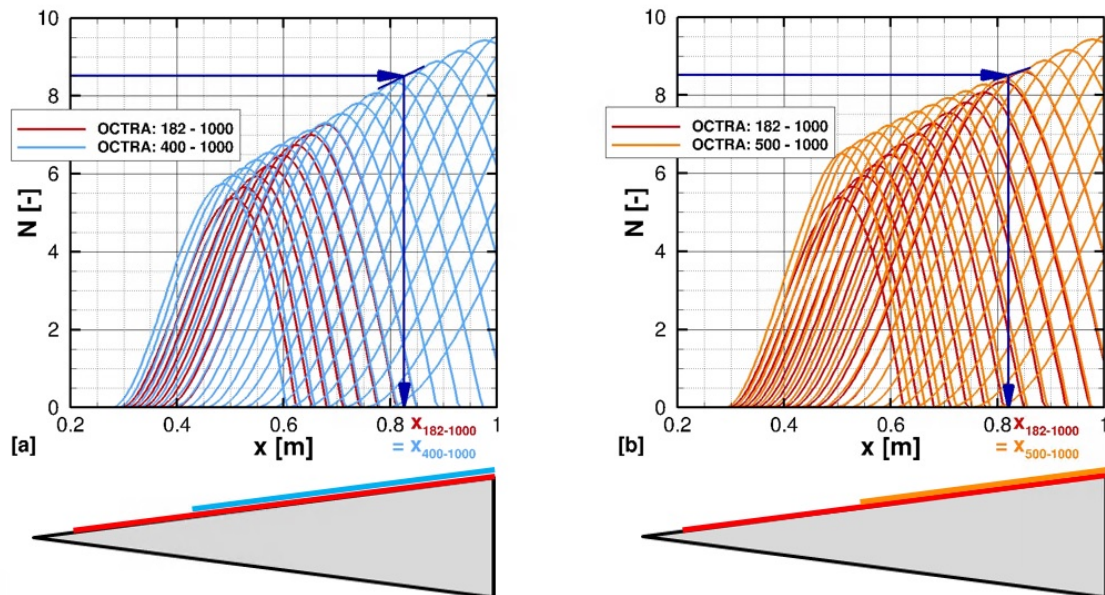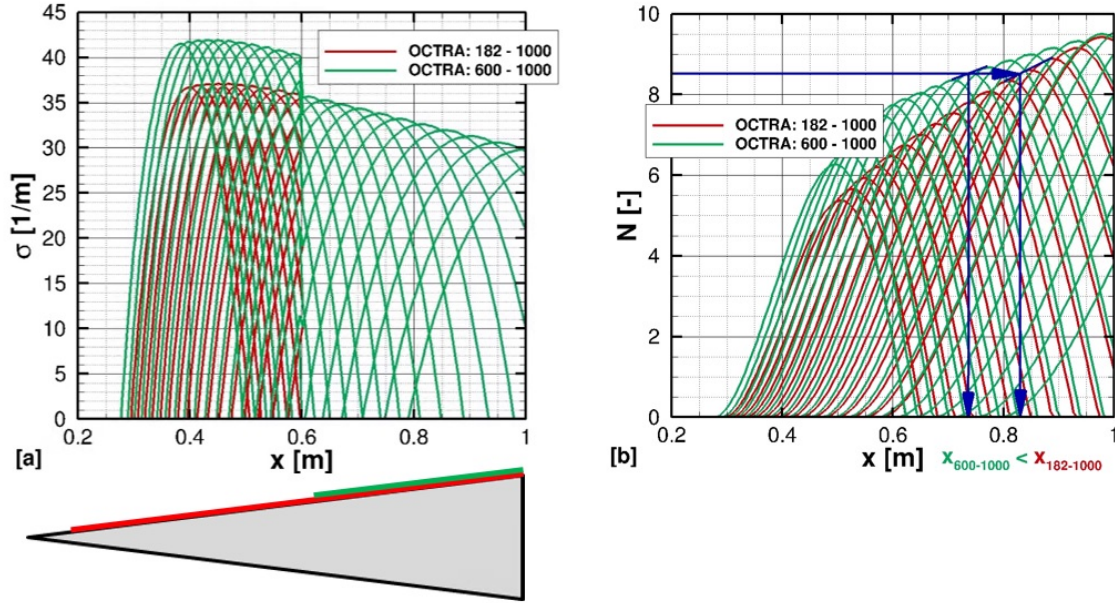

Fig 4. Variation of the insert length: 400 mm - 1000 mm (blue lines), 500 mm - 1000 mm (orange lines), $Re_m = 6.4 \times 10^6$/m.

Fig 5. Variation of the insert length: 600 mm - 1000 mm (green lines), $Re_{\mathrm{m}} = 6.4 \times 10^6/\mathrm{m}$.

numerical recommendation for the start of the insert is $x \leq 500$mm, which delivers the same predicted transition start as an insert with maximal insert length for the investigated Reynolds number. For the HEG test campaign, different free stream conditions with varied freestream unit Reynolds numbers were planned / performed, thus finally an insert with a starting x of 305 mm is chosen. This reduced insert length offers a sufficient effectiveness for the whole selected Reynolds number range of table 2.

4. Numerical predictions versus measurements

This section summarises the comparison of the NOLOT calculations with the HEG measurements, analysing the transition shift due to the second mode damping as well as the second mode damping itself.

4.1. Comparison of the transition delay

The cone was tested in a unit Reynolds numbers range of $Re_{\mathrm{m}} = 1.4 \times 10^6/\mathrm{m}$ to $Re_{\mathrm{m}} = 6.4 \times 10^6/\mathrm{m}$ (table 2). For the analysis of the measured transition, figure 6 provides the normalized heat flux distribution on the solid reference surface (lines with rectangle symbols) and the porous surface: CC (dashed lines with triangle symbols) and OCTRA (long-dashed lines with circle symbols). The test cases with the lowest Reynolds number ($Re_{\mathrm{m}} = 1.4 \times 10^6/\mathrm{m}$) show a laminar behaviour independent of the surface material. These cases are performed for the second mode comparison, which are summarized in section 4.2. For the analyses of the transition prediction the unit Reynolds numbers $Re_{\mathrm{m}} = 4.0 \times 10^6/\mathrm{m}$ and $Re_{\mathrm{m}} = 6.4 \times 10^6/\mathrm{m}$ are chosen. For these Reynolds numbers the heat fluxes increase due to boundary layer transition looking at the measurements of the smooth reference surface side. The effect of the porous material is also clearly visible: the increased heat flux is shifted downstream to a higher local model length. For the improved OCTRA material the effect increases, compared to the C/C material. This is observable for both Reynolds numbers.

Furthermore, it can be seen in figure 6 that the heat flux measurements on the porous surface have higher scatter compared to the solid surface. This has already examined in [9]: Contrary to a solid steel surface, the coaxial thermocouples cannot be integrated into a porous ceramic by polishing the transducer head. This would cause significant damage to the porous material making it unusable for its design purpose. For this reason, minor transducer misalignment had to be accepted although the
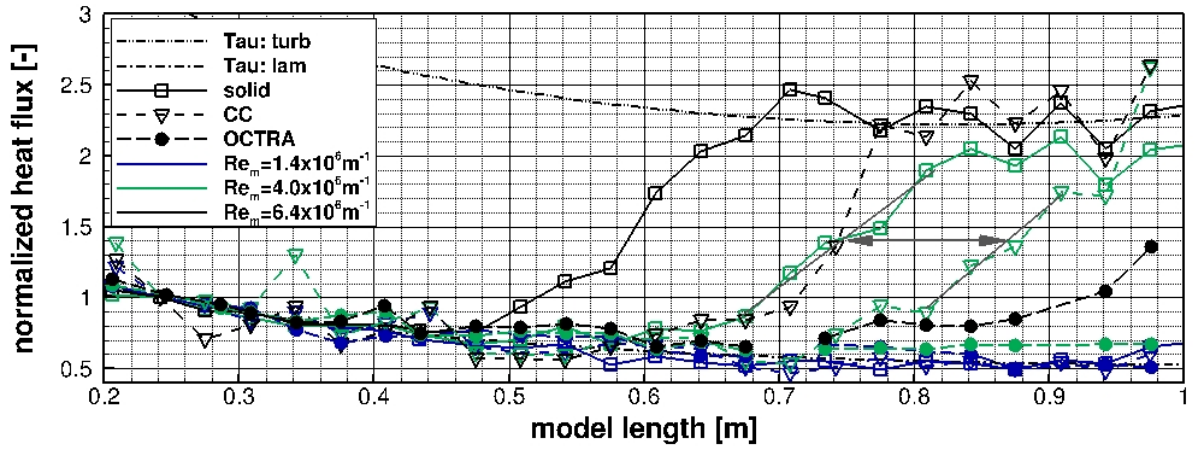
Fig 6. Normalized heat flux distribution on solid and porous surface.

integration was carried out with great care. Due to scatter of the heat flux data on the porous surface it is not obvious where to define the beginning of transition on the cone with porous insert. Thus a linear fit was introduced to represent the characteristic slope of the heat flux close to the end of transition [26]. This issue is illustrated exemplary in figure 6 for the CC test case with $Re_{\mathrm{m}} = 4.0 \times 10^6$/m (gray lines and arrow). The mean relative displacement of the two fits was calculated and summarized in table 3, which is discussed in the following together with the numerical results.

Table 3. Comparison: Transition delay - numerics/experiments.

Re_m [10^6/ m]	$(Re_{\mathrm{trans,porous}} - Re_{\mathrm{trans,smooth}})/Re_{\mathrm{trans,smooth}}$			
	C/C: Exp.	C/C: LST	OCTRA: Exp	OCTRA: LST
4.0	0.15 [26]	0.13 [9]	laminar	laminar
6.0	0.20 [26]	0.15 [9]	0.35	0.24

The rows, which includes the C/C material results of table 3, have already been published in [26], [9]. The results are added to confirm the improvement of the OCTRA material. As already mentioned in section 3.3, for the LST prediction of the numerical, relative transition delay, the semiempirical approach of the e^N-method is applied. Please note, usually the measured beginning of the transition is used for this kind of LST prediction to have a standard $N_{\mathrm{trans,smooth}}$ value for the comparison between different wind tunnels. Consequently, the here defined experimental x-positions of fig. 6 results in a higher $N_{\mathrm{trans,smooth}}$ value than usual.

Beginning with the lower Reynolds number of $Re_{\mathrm{m}} = 4.0 \times 10^6$/m, the measured transition x-coordinate of the solid surface side of fig. 6 results in a $N_{\mathrm{trans,smooth}}$ of about 8 (see fig. 7.a). This $N_{\mathrm{trans,smooth}}$ of 8 is used in fig. 7.b for the prediction of the transition shift due to the porous material. The calculations of the C/C material is marked by red color and the improved OCTRA material by green color. The second mode damping of the OCTRA material is significantly higher, compared to the C/C material. Consequently, the resulting predicted transition shift is also larger: in fig. 7.b results the improvement in a predicted laminar behaviour.

To be consistent within the paper the measured x-position of fig. 6 was also used for the test case of sec-

tion 3.3 ($Re_\mathrm{m} = 6.4 \times 10^6$/m), which results in an $N_\mathrm{trans,smooth} = 8.5$ for the smooth surface side, which is consequently also applied in this section. Figure 8 depicts the numerical results for $Re_\mathrm{m} = 6.4 \times 10^6$/m. As expected, the predicted shift for the recent, optimized OCTRA material is also for this test case larger than for C/C.

Table 3 summarized the comparison of the predicted and measured transition delay. For the OCTRA material at the lower unit Reynolds number $Re_\mathrm{m} = 4.0 \times 10^6$/m the increase of the shift due to the material is so high, that the flow is adjusted to a completely laminar status in the experiments as well as in the predictions. For the Reynolds number $Re_\mathrm{m} = 6.4 \times 10^6$/m the shift of the transition increases applying the improved OCTRA, looking at the experiments as well as the numerical predictions. The detailed analysis of the C/C material can be found in [26], [9]. For the OCTRA NOLOT predicts a lower second mode damping, compared to the experiments. These differences are investigated in more detail by looking at the second mode comparison (see next section 4.2).
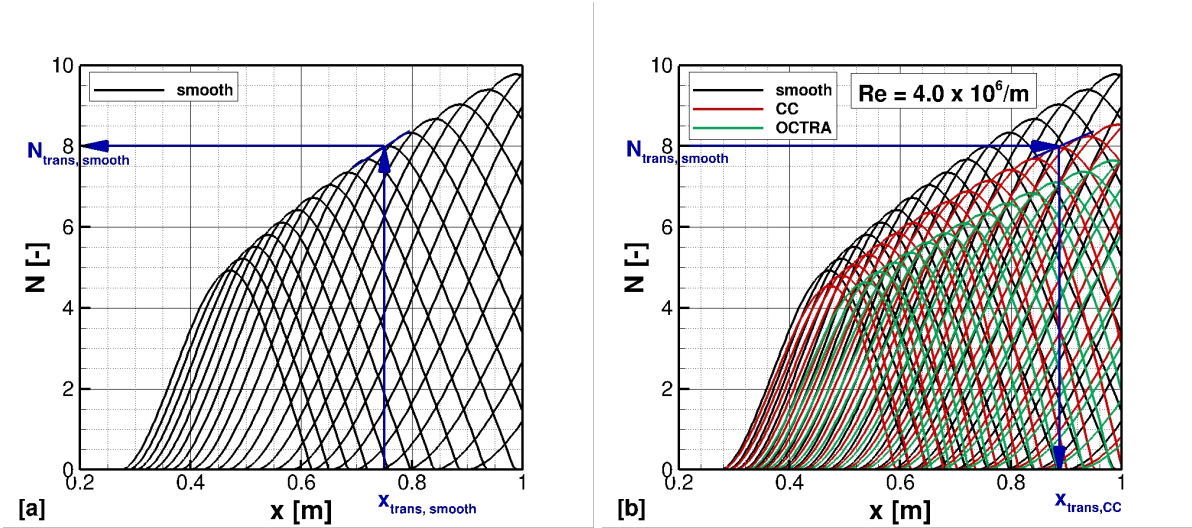

Fig 7. Transition prediction using e^N-method, $Re_\mathrm{m} = 4.0 \times 10^6$/m.

4.2. Comparison of the second modes

Two requirements are necessary to compare the numerically obtained second mode amplitude against experimental data: First, the signal to noise ratio of the second mode instability at the PCB sensor position has to be high enough. Second, the flow at the sensor position has to be laminar. Otherwise, a decomposition of the second mode due to the transition process is possible which does not allow to compare the measurements with the linear, laminar predictions of NOLOT. Thus, a test case with a low unit Reynolds number is chosen: $Re_\mathrm{m} = 1.4 \times 10^6$/m (see table 2). For this free stream condition at all selected sensor positions ($x = 0.650\,$m and $x = 0.785$) a laminar boundary layer was observed (see fig. 6 for the visualisation of the laminar behavior) and the second mode is clearly measurable.

Figure 9 provides the second modes at the selected PCB sensor positions: a) $x = 0.650\,$m and b) $x = 0.785\,$m. On the right ordinate figure 9 shows the measured amplitude spectral density (ASD). It was derived by conducting a discrete Fourier transformation of the measured pressure fluctuations recorded in the test time, as a function of the measured frequency marked as symbols. The measurements on the smooth surface are marked with black color, the measurements on the porous C/C surface with red and on the porous OCTRA surface with blue. The same colors are used for the LST calculations ($e^N = f(f)$). As expected, the calculated/measured second mode is amplified in streamwise direction. Due to the increase of the boundary layer thickness the frequencies of the second modes are shifted to lower values, which can be explained with the following relation between the boundary layer thickness δ
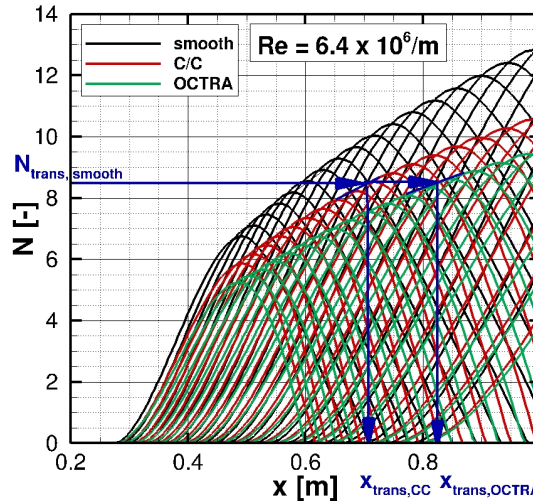
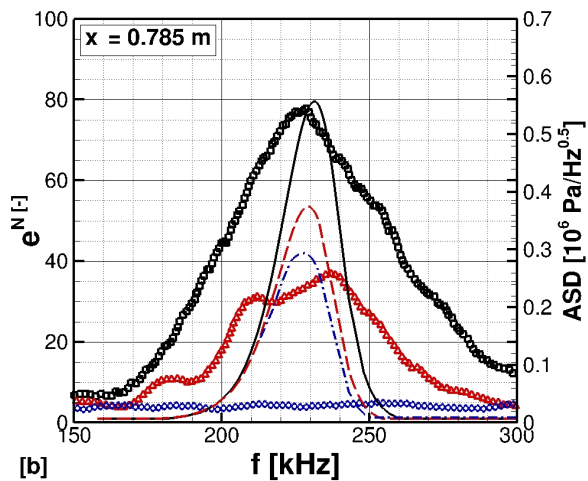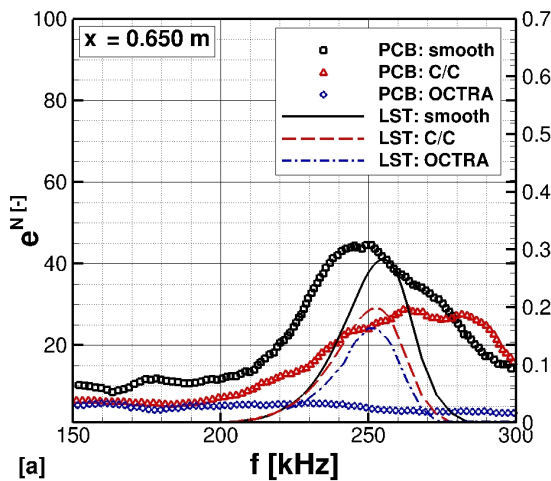**Fig 8.** Transition prediction using e^N-method, $Re_{\mathrm{m}} = 6.4 \times 10^6$/m.

Fig 9. Second mode comparison, $Re_{\mathrm{m}} = 1.4 \times 10^6$/m

.

and the wavelength λ [1]: $\lambda \approx 2\,\delta$.

The measured ASD data cannot be compared directly with the numerically calculated e^N-values. However, it is possible to compare the damping of the second mode and its frequency range. The comparison of the calculated/measured frequency range (using the peak frequencies) shows a difference of less 5 % which is in good agreement. Analysing the damping of the second modes due to the C/C material, was already analysed in [9]. This data are added here for completeness and to demonstrate the improved behaviour of the new OCTRA material: The measured/calculated damping of second mode is higher on the OCTRA surface as on the CC surface. In the experiments at the selected sensor positions the second modes are completely damped or in the range of the background noise level. The LST delivers the same trend: the damping of the second mode from the numerically-rebuilt OCTRA material is higher than for the C/C material. Nevertheless, applying OCTRA the measured damping is higher than the predicted, which corresponds to the larger shift of the transition location in the previous section 4.1. These differences are discussed in the next section 4.3.

4.3. Variation of the porosity

A possible explanation for visible higher second mode damping in the experiments compared to the numerical predictions is the porosity. Computer tomography scans were performed taking scans of the OCTRA surface. The result indicates that the surface has a higher porosity than the deeper layer. This increased porosity at the surface has a significant influence on the acoustic behaviour. A varied porosity depending on the depth can not be simulated with the chosen numerical approach. Nevertheless, in this section the LST approach is used to give an impression of the influence of the chosen porosity on the second mode damping. The test case of figure 8 is chosen: $Re_\mathrm{m} = 6.4 \times 10^6$/m. Instead of a varied porosity depending on the depth, the constant porosity is varied to match the measured/predicted transition shift of $\delta x = 0.35$ (table 3). A constant porosity of about 21%, marked by orange color in fig. 10 instead of the original applied 16% (green color) results in an match of the measured/predicted transition shift.
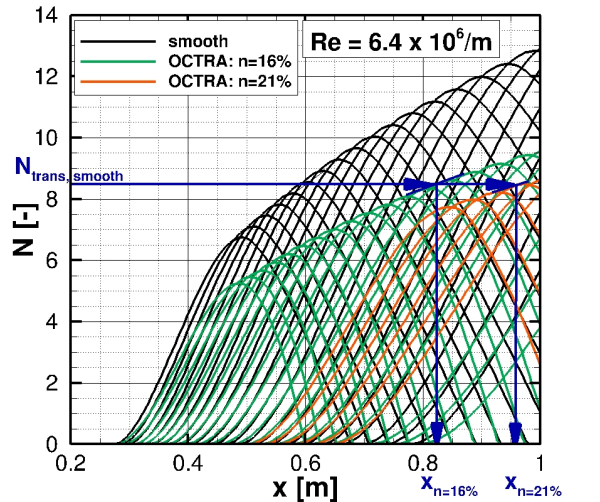

Fig 10. Variation of the porosity, $Re_\mathrm{m} = 6.4 \times 10^6$/m.

5. Conclusion

A new temperature stable porous carbon fiber reinforced silicon carbide (OCTRA) material (Dittert et al. [14]) is investigated in the current paper. As model a 7° half-angle blunt cone with nose radius of 2.5 mm at a unit Reynolds numbers range between $Re_\mathrm{m} = 1.4 \times 10^6$/m to $Re_\mathrm{m} = 6.4 \times 10^6$/m and low total enthalpy is analysed.

The numerical predictions for the OCTRA material deliver a lower damping of the second modes and consequently also a lower transition shift as visible in the measurements. The most likely explanation is the measured varied porosity over the depth of the OCTRA material. A varied porosity cannot be simulated with the chosen numerical LST approach. Thus a variation of a constant porosity is investigated to deliver at least an impression of the effect of the porosity on the damping of the second mode. An increase from 16% to 21% is applied, which results in a match between numerical predictions and measurements of the selected test case. A complete reproduction of a varied porosity over the depth is only with direct numerical simulations (DNS) possible and recommended.

Nevertheless, an improvement of the new OCTRA material, compared with the preceding C/C material, is demonstrated: a significant higher second mode damping and consequently a larger transition delay is shown numerically as well as experimentally. In summary it can be written, that the improved OCTRA material is successfully investigated for the application as ultrasonically absorber.

References

[1] Mack, L. M., "Boundary layer linear stability theory," *AGARD - Special Course on Stability and Transition of Laminar Flow*, 1984.

[2] Fedorov, A. V., Malmuth, N. D., Rasheed, A., and Hornung, H. G., "Stabilization of Hypersonic Boundary Layers by Porous Coatings," *AIAA*, Vol. 39, No. 4, 2001, pp. 605–610.

[3] Rasheed, A., Hornung, H. G., Fedorov, A. V., and Malmuth, N. D., "Experiments on Passive Hypervelocity Boundary-Layer Control Using an Ultrasonically Absorptive Surface," *AIAA*, Vol. 40, No. 3, 2002, pp. 481–489.

[4] Fedorov, A. V., Shiplyuk, A., Maslov, A., Burov, E., and Malmuth, N., "Stabilization of a hypersonic boundary layer using an ultrasonically absorptive coating," *Journal of Fluid Mechanics*, Vol. 479, 2003, pp. 99–124. doi:10.1017/S0022112002003440.

[5] Maslov, A., Shiplyuk, A., Sidorenko, A., Polivanov, P., Fedorov, A., Kozlov, V., and Malmuth, N., "Hypersonic Laminar Flow Control Using a Porous Coating of Random Microstructure," *44th AIAA Aerospace Sciences Meeting and Exhibit*, Reno, Nevada, 2006. AIAA 2006-1112.

[6] Maslov, A. A., Fedorov, A. V., Bountin, D. A., Shiplyuk, A. N., Sidorenko, A. A., Malmuth, N., and Knauss, H., "Experimental study of transition in hypersonic boundary layer on ultrasonically absorptive coating with random porosity," *46th AIAA Aerospace Sciences Meeting and Exhibit*, Reno, Nevada, 2008. AIAA 2008-587.

[7] Lukashevich, S. V., Morozov, S. O., and Shiplyuk, A. N., "Experimental study of the effect of a passive porous coating on disturbances in a hypersonic boundary layer 1. Effect of the porous coating length," *Journal of Applied Mechanics and Technical Physics*, Vol. 54, No. 4, 2013, pp. 572–577. doi:10.1134/S002189441304007X.

[8] Wagner, A., Hannemann, K., Wartemann, V., and Giese, T., "Hypersonic boundary-layer stabilization by means of ultrasonically absorptive carbon-carbon material - Part 1: Experimental Results," *51st AIAA Aerospace Sciences Meeting*, Texas, 2013. doi:10.2514/6.2013-270, AIAA2013-0270.

[9] Wartemann, V., Wagner, A., Kuhn, M., Eggers, T., and Hannemann, K., "Passive hypersonic boundary layer transition control using an ultrasonically absorptive coating with random microstructure: Computational analysis based on the ultrasonic absorption properties of carbon-carbon," Elsevier, 2015. doi: 10.1016/j.piutam.2015.03.068.

[10] Weihs, H., "Sounding Rockets for Entry Research: SHEFEX Flight Test Program," *21st ESA Symposium on European Rocket and Balloon Programmes and related Research*, Vol. Vol. SP-721, ESA, 2013.

[11] Reimer, T., "The KERAMIK Thermal Protection System Experiment on the FOTON-M2 Mission," *Thermal Protection Systems and Hot Structures (5th Workshop)*, ESA, 2006.

[12] Zuber, C., Reimer, T., Stubicar, K., Heidenreich, B., and Hald, H., "Manufacturing of the CMC nose cap for the EXPERT spacecraft," *ICACC*, 2010.

[13] Dittert, C., and Kütemeyer, M., "Octra - Optimized Ceramic for Hypersonic Application with Transpiration Cooling," *Advances in High Temperature Ceramic Matrix Composites and Materials for Sustainable Development*, Vol. 263, 2017. doi:10.1002/9781119407270.ch37.

[14] Dittert, C., Kütemeyer, M., Kuhn, M., and Wagner, A., "Process Optimization of Ceramic Matrix Composites for Ultrasonically Absorptive TPS Material," *AIAA Aviation, Joint Thermophysics and Heat Transfer Conference*, 2018. doi:10.2514/6.2018-2947.

[15] Mack, A., and Hannemann, V., "Validation of the Unstructured DLR-TAU-Code for Hypersonic Flows," *32nd AIAA Fluid Dynamics Conference and Exhibit*, St. Louis, Missouri, 2002. AIAA 2002-3111.

[16] Schwamborn, D., Gerhold, T., and Heinrich, R., "The DLR Tau-code: Recent Applications in Research and Industry," *European Conference on Computational Fluid Dynamics ECCOMAS CFD*, 2006.

[17] Reimann, B., and Hannemann, V., "Numerical Investigation of Double-Cone and Cylinder Experiments in High Enthalpy Flows using the DLR TAU code," *48th AIAA Aerospace Sciences Meeting Including the New Horizons Forum and Aerospace Exposition*, 2010. doi:10.2514/6.2010-1282.

[18] Wartemann, V., Wagner, A., Wagnild, R., Pinna, F., Miró, F. M., Tanno, H., and Johnson, H., "High enthalpy effects on hypersonic boundary layer transition," *Journal of Spacecraft and Rockets*, Vol. 56, No. 2, 2019. doi:10.2514/1.A34281.

[19] Wagner, A., Hannemann, K., and Kuhn, M., "Ultrasonic absorption characteristics of porous carbon-carbon ceramics with random microstructure for passive hypersonic boundary layer transition control," *Experiments in Fluids*, Vol. 55, No. 6, 2014, 1750. doi:10.1007/s00348-014-1750-4, URL `http://dx.doi.org/10.1007/s00348-014-1750-4`.

[20] Hein, S., Bertolotti, F. P., Simen, M., Hanifi, A., and Henningson, D., "Linear nonlocal instability analysis - the linear NOLOT code," Tech. Rep. IB-223-94 A56, DLR, 1994.

[21] Wartemann, V., Wagner, A., Kuhn, M., Eggers, T., and Hannemann, K., "Passive hypersonic boundary layer transition control using an ultrasonically absorptive coating with random microstructure: Computational analysis based on the ultrasonic absorption properties of carbon-carbon," *IUTAM ABCM Symposium on Laminar Turbulent Transition*, 2014.

[22] Maslov, A., "Experimental and Theoretical Studies of Hypersonic Laminar Flow Control Using Ultrasonically Absorptive Coatings (UAC)," Tech. rep., ISTC 2172-2001, 2003.

[23] Wartemann, V., Wagner, A., Kuhn, M., Eggers, T., and Hannemann, K., "Passive hypersonic boundary layer transition control using an ultrasonically absorptive coating with random microstructure: Computational analysis based on the ultrasonic absorption properties of carbon-carbon," Elsevier, 2015. doi: 10.1016/j.piutam.2015.03.068.

[24] Möser, M., *Technische Akustik*, 2012.

[25] Hannemann, K., Martinez Schramm, J., and Karl, S., "Recent extensions to the High Enthalpy Shock Tunnel Göttingen (HEG)," *2nd International ARA Days*, Arcachon, France, 2008.

[26] Wagner, A., "Passive Hypersonic Boundary Layer Transition Control Using Ultrasonically Absorptive Carbon-Carbon Ceramic with Random Microstructure," Ph.D. thesis, Katholieke Universiteit Leuven, 2014.